

Surface Reconstruction of Amorphous Ni—Co—S—O Material with a Functional Gradient Layer for Highly Efficient and Stable Alkaline Hydrogen Evolution

Lijuan Liu, Yingqiu Zheng, Wenshu Chen,* Yongping Du, Linfeng Hu, Guoqiang Luo, Qiang Shen, and Jian Zhang*

Alkaline water electrolysis holds potential for large-scale, high-purity hydrogen production. However, the slow kinetics of water dissociation and challenging conditions in alkaline environments complicate the search for an electrocatalyst with both high activity and durability. In this study, a highly active and stable amorphous electrocatalyst is introduced, 3Ni—Co—S—O, developed via a straightforward electrodeposition method for alkaline hydrogen evolution reaction (HER). Notably, the surface of the 3Ni—Co—S—O catalyst undergoes a compositional reconstruction during alkaline HER, yet maintains its amorphous structure. This reconstruction spans roughly 6 μm , leading to a gradual decrease in Ni and S content and a corresponding increase in O concentration toward the surface, thereby forming a stable, gradient active layer. Benefitting from this layer and its amorphous nature, the 3Ni—Co—S—O catalyst demonstrates superior alkaline HER activity—requiring only 170 mV to achieve an industrial HER current density of 1000 mA cm⁻². It also showcases remarkable stability, with a mere 15 mV increase in overpotential during continuous HER at 300 mA cm⁻² for 24 h, outperforming the commercial Pt/C catalyst. The research provides a novel approach to designing high-performance amorphous alkaline HER electrocatalysts cost-effectively and contributes insights for understanding and developing advanced amorphous catalysts across various applications.

1. Introduction

Hydrogen serves as a crucial energy carrier and industrial raw material, employed in diverse sectors such as oil refining, ammonia production, and industrial fuel cells.^[1] The production of hydrogen from water electrolysis emerges as a notably promising technology for green hydrogen production.^[2] Among its various methodologies, alkaline electrolytic hydrogen production has garnered significant attention, attributed to its myriad advantages including limitless reactant availability, elevated manufacturing safety, consistent output, and high product purity.^[3] However, the intrinsic reaction kinetics of alkaline hydrogen evolution reaction (HER) is inherently slow due to the high energy barrier associated with the initial step of water splitting—water dissociation.^[4] Consequently, the quest for low-cost, efficient, and stable alkaline HER electrocatalytic materials remains fraught with challenges.^[5]

Researchers have pioneered the development of non-precious, metal-based

L. Liu, J. Zhang
State Key Laboratory of Advanced Technology for Materials Synthesis and Processing
Wuhan University of Technology
Wuhan 430070, P. R. China
E-mail: zhangjian178@whut.edu.cn

L. Liu, Y. Zheng, J. Zhang
Chaozhou Branch of Chemistry and Chemical Engineering Guangdong Laboratory
Chaozhou 521000, P. R. China

W. Chen, L. Hu
School of Materials Science and Engineering
Southeast University
Nanjing 211189, P. R. China
E-mail: 101013800@seu.edu.cn

Y. Du
MIIT Key Laboratory of Semiconductor Microstructure and Quantum Sensing
Nanjing University of Science and Technology
Nanjing 210094, P. R. China

Y. Du
Department of Applied Physics
Nanjing University of Science and Technology
Nanjing 210094, P. R. China

G. Luo, Q. Shen
State Key Lab of Advanced Technology for Materials Synthesis and Processing
Wuhan University of Technology
Wuhan 430070, P. R. China

 The ORCID identification number(s) for the author(s) of this article can be found under <https://doi.org/10.1002/sml.202502293>

DOI: 10.1002/sml.202502293

alkaline HER catalysts, mainly including transition metal sulfides,^[6] oxides,^[7] and phosphides.^[8] Of the myriad catalysts studied, transition metal chalcogenides have demonstrated superior performance in terms of activity and stability, positioning them as promising electrocatalysts for alkaline HER.^[9] To further enhance their HER catalytic functionality and dynamics, several strategies such as doping,^[10] compositing,^[11] and alloying^[12] have been employed. These techniques effectively boost their performance in alkaline hydrogen evolution. However, the preparation processes typically utilized are intricate, often necessitating high synthesis temperatures. Furthermore, the activity of these materials still requires enhancement to achieve efficient alkaline HER.^[13]

Recent discoveries have revealed that amorphous materials, such as CoMoP_x,^[14] MoS₂,^[15] Pd₃P₂S₈,^[16] and MoNi/NiMoOx^[17] exhibit high HER activity. Their superior catalytic performance, compared to crystalline functional catalysts, is primarily attributed to the abundance of catalytic active sites.^[18] These sites mainly consist of a large number of defects and unsaturated coordination structures, which enhance the intrinsic catalytic activity of the material and increase its electrochemical active surface area.^[19] Current methods for obtaining amorphous HER electrocatalysts include Chemical Vapor Deposition (CVD),^[20] hydrothermal method,^[21] and powder metallurgy.^[22] However, these methods are often time-consuming, and while the catalytic materials prepared through amorphization strategies demonstrate high HER activity, they suffer from poor stability. The electrodeposition technique is a simple yet efficient method, extensively employed in the synthesis of amorphous catalysts.^[23] However, research into the structural evolution process of amorphous catalysts during HER and its relationship with the catalytic activity and stability of the material should be deepened. This will aid in the preparation of more efficient and stable amorphous electrocatalysts for alkaline HER.

In this work, we synthesized self-supported amorphous Ni–Co–S–O-based materials on nickel foam surfaces using a straightforward one-step electrodeposition technique for alkaline HER (Figure 1a). During the alkaline HER process, it was observed that the catalyst's surface underwent component reconstruction, leading to the formation of a surface gradient component layer ≈6 μm in thickness. Specifically, across the surface gradient layer, the content of Ni and S elements progressively decreased, while the O element content correspondingly increased, all while maintaining its amorphous characteristics. Remarkably, this gradient amorphous component surface layer demonstrated efficient and stable alkaline HER. Upon optimization, the as-designed sample of 3Ni–Co–S–O (with the specific elemental composition of Ni_{5.3}Co_{1.4}S_{1.2}O₁) exhibits the best alkaline HER activity after surface component reconstruction, which only required overpotentials of merely 104, 142, and 170 mV to drive HER current densities of 100, 500, and 1000 mA cm⁻², respectively. Moreover, it exhibited a low Tafel slope of 31.0 mV dec⁻¹ in 1 M KOH and impressive stability, operating consistently for 24 h under a hydrogen evolution current density of 300 mA cm⁻². This research not only offers a potent, stable, and cost-effective electrocatalyst for alkaline HER but also lays a foundational theoretical framework for investigating surface structural evolution and stability enhancement

in high-performance amorphous catalytic materials for related applications.

2. Results and Discussion

2.1. Synthesis and Characterizations

The synthesis of the Ni–Co–S–O-based catalyst is depicted in Figure 1a. The procedure commenced with the preparation of a solution comprising Ni, Co, S, and O elements. Subsequently, the constant current electrodeposition technique was employed to fabricate Ni–Co–S–O-based catalysts on nickel foam (NF) surfaces. The electrodeposition process primarily entails a synergistic regulation of ion migration behavior, governed by three driving forces: concentration gradient, electric field force, and chemical reaction. Under the influence of an applied electric field, cations such as Ni²⁺ and Co²⁺, and anions such as S²⁻, SO₄²⁻, and OH⁻ exhibit contrasting migration directions. However, ion reaction kinetics proximate to the cathode surface is not constrained by this migration direction. Consequently, both anions and cations can simultaneously partake in reactions on the foam nickel surface. As metal ions undergo continuous reduction on the cathode surface, a localized concentration gradient is formed, prompting anions to diffuse toward the cathode.^[24] This overcomes the electric field's repulsive effect, enabling anions to participate in reactions on the foam nickel surface. Moreover, water molecules and thiourea molecules in the solution undergo electrochemical reduction on the cathode surface, generating active S²⁻ and OH⁻ species that contribute to the reaction. The cumulative effect of these multiple driving mechanisms results in a uniform Ni–Co–S–O composite layer being deposited on the cathode surface (foam nickel substrate). This process is readily characterized by the color change of the substrate from silvery white to black. By adjusting the initial Ni to Co elemental ratio, we synthesized Ni–Co–S–O-based catalysts with varying Ni–Co proportions, including 9Ni–Co–S–O, 6Ni–Co–S–O, 3Ni–Co–S–O, Ni–Co–S–O, Ni–S–O, and Co–S–O (refer to the Experimental Section). To assess the crystallinity of the synthesized Ni–Co–S–O samples, X-ray diffraction (XRD) analyses were performed (Figure 1b). The diffraction peaks at 44.60° and 51.98° can be attributed to the (111) and (200) crystal planes of nickel metal (JCPDS no.70-0989), respectively. Apart from these two distinct nickel metal diffraction peaks, no other peaks were identified in the synthesized samples, suggesting the amorphous nature of the electrodeposited products on the NF substrate.

Raman spectroscopy experiments were conducted to elucidate the bonding characteristics of the synthesized Ni–Co–S–O-based samples, as shown in Figure 1c. The vibrational modes corresponding to Co–S and Co–O bonds are evident in the Co–S–O sample, suggesting a relatively strong association between Co and both S and O elements within this sample. In contrast, for the Ni–S–O and other Ni–Co–S–O-based samples, only the vibrational mode associated with the Ni–S bond is discernible, indicating a pronounced interaction between Ni and S elements but a minimal one between Ni and O. It is noteworthy that sulfur plays a pivotal role in the hydrogen evolution reaction (HER) due to the high electronegativity of sulfur atoms in metal sulfides. This electron-withdrawing capacity enhances the adsorption of positively charged intermediates during HER, thereby conferring

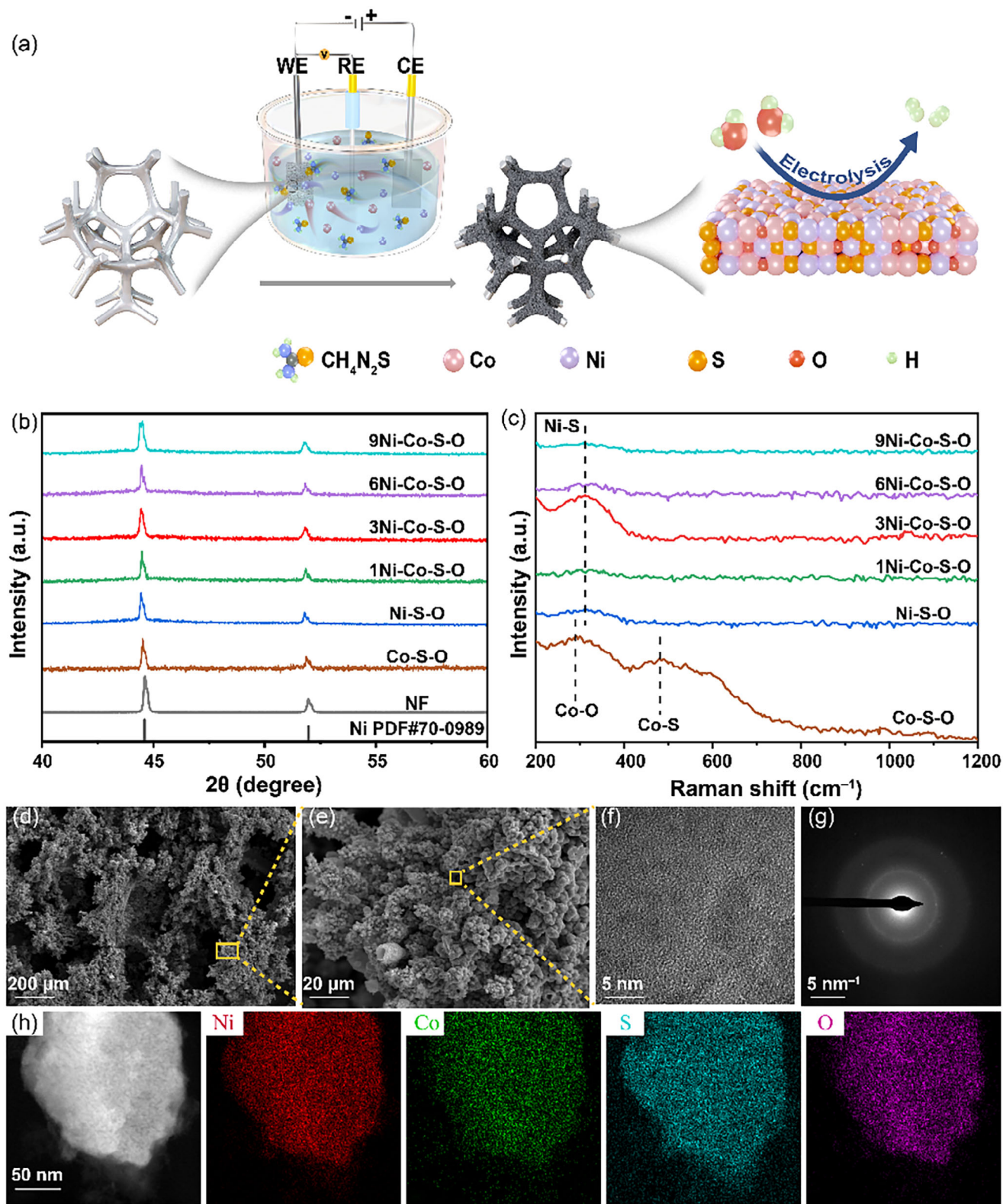


Figure 1. Synthesis and characterizations. a) A schematic of the synthetic process through electrodeposition and HER application of the amorphous Ni–Co–S–O-based materials. b) XRD patterns. c) Raman spectra. d,e) SEM images, f) TEM image, g) SAED pattern, and h) HAADF-STEM image and corresponding EDS-Mapping results of the synthesized 3Ni–Co–S–O material.

robust catalytic activity. Significantly, the 3Ni–Co–S–O sample exhibits the most pronounced Raman signal for Ni–S bonding, underscoring the strongest interaction between Ni and S elements among the studied samples. This attribute is likely to be beneficial for both HER activity and stability. Consequently, the 3Ni–Co–S–O sample was chosen for further characterization as a representative example.

Scanning electron microscopy (SEM) was employed to analyze the surface morphology of the 3Ni–Co–S–O catalyst. The SEM images revealed that post-electrodeposition, the NF substrates were consistently coated with a coarse yet intact layer of nano products, culminating in a continuous 3D porous structure (Figure 1d,e; Figure S1, Supporting Information). This particular surface morphology can markedly enhance the specific surface area of the catalysts and the bubble transfer rate, thereby improving the HER activity and kinetics. Subsequent use of the transmission electron microscope (TEM) allowed for an observation of the sample's microstructure. It was noted that the 3Ni–Co–S–O sample exhibited no lattice stripes under high-resolution TEM observation (Figure 1f), nor any distinct patterns in the selective electron diffraction (SEAD) experiment (Figure 1g). In conjunction with the XRD results, it was concluded that the electrodeposition products are primarily amorphous. The SEM-coupled energy-dispersive X-ray spectrometer (EDS) results were used to calculate the elemental concentrations in the samples (Figure S2 and Table S1, Supporting Information). The results indicated that the specific chemical formula of the 3Ni–Co–S–O sample is $\text{Ni}_{5.3}\text{Co}_{1.4}\text{S}_{1.2}\text{O}_1$. The high-angle annular dark field scanning TEM (HAADF-STEM) image and corresponding EDS mapping results demonstrated a uniform distribution of the Ni, Co, S, and O elements within the samples (Figure 1h).

In order to gather a more precise understanding of the coordination modes and electronic surroundings of distinct atoms within the representative amorphous 3Ni–Co–S–O sample, we conducted X-ray absorption spectroscopy (XAS) analyses. Figure 2a presents the Ni K-edge x-ray absorption near edge structure (XANES) spectra for the prepared 3Ni–Co–S–O, Ni foil, NiO, and NiS samples. It is evident that the absorption energy (E_0) of the Ni element within the 3Ni–Co–S–O sample closely aligns with that of the Ni foil, suggesting that the Ni atoms predominantly exist in a metallic state. To delve deeper into the local structure of Ni atoms, we procured the k²-weighted extended x-ray absorption fine structure (EXAFS) spectra of the Ni k-edge through the Fourier transform (Figure 2b). The observed peaks at 2.18, 1.93, 1.63, and 2.55 Å are attributed to Ni–Ni, Ni–S, Ni–O, and Ni–O–Ni coordination, respectively. The 3Ni–Co–S–O sample features a primary peak at 2.10 Å, suggesting that the Ni atom primarily forms bonds with metallic atoms, resulting in a Ni–Ni/Co bond. The broad peak and negative offset position for the 3Ni–Co–S–O could be influenced by the presence of S, implying the existence of Ni–S coordination. The diminished peak intensity for the 3Ni–Co–S–O is largely attributed to the sample's amorphous structure.^[25] The structural parameters derived from the fitting of EXAFS spectra provide detailed insights into the local coordination environments and bonding properties of Ni and Co atoms in the synthesized 3Ni–Co–S–O catalyst (Figure 2c; Figure S3a, and Table S2, Supporting Information). Fitting results indicate that each Ni

atom has a coordination number of four, interacting with one sulfur atom (with a Ni–S bond length of 2.23 Å), one Ni atom (with a Ni–Ni bond length of 2.40 Å), and two Co atoms (each with a Ni–Co bond length of 2.54 Å). This arrangement suggests that within the catalyst, Ni atoms predominantly exhibit Ni–S and Ni–Ni/Co bonding, establishing a stable local coordination environment. Additional bonding details of Ni are visually demonstrated through the small wavelet transformation, where the 3Ni–Co–S–O sample exhibits a pronounced Ni–Ni/Co peak and a subtle Ni–S peak, reaffirming that Ni predominantly exists in a metallic state (Figure 2e).

In addition to Ni, the XANES and EXAFS spectra of the Co K-edge are presented in Figure 2c,d, respectively. As with Ni, the E_0 of the Co element in the 3Ni–Co–S–O sample closely aligns with that of the Co foil, suggesting that the Co atoms predominantly exist in a metallic state. The local coordination environment of Co was further explored using Fourier transforms of the Co K-edge EXAFS spectra. As illustrated in Figure 2d, the peaks at 2.18, 1.87, 1.66, and 2.58 Å are attributed to Co–Co, Co–S, Co–O, and Co–O–Co coordination, respectively. The primary peak of the 3Ni–Co–S–O sample at 2.07 Å is indicative of Co–Co/Ni coordination. Notably, this peak exhibits a broad shape and a negative offset position, suggesting the presence of Co–S coordination. As revealed by the fitting results in Figure 2f and Figure S3b, and Table S2 (Supporting Information), the Co atom has a coordination number of four, coordinating with one S atom (with a Co–S bonding length of 2.24 Å), two Ni atoms (with each Co–Ni bond length of 2.36 Å) and one Co atom (with a Co–Co bond length of 2.53 Å), respectively. This coordination data confirms the bonding network of Co atoms with adjacent Ni/Co and S atoms within the catalyst. The binding details of Co are further clarified by the small wavelet transform (Figure 2f) and results show that the 3Ni–Co–S–O sample displays a pronounced Co–Co/Ni peak and a subtle Co–S peak, confirming that Co predominantly exists in a metallic state.

2.2. Electrocatalytic HER Performance

The alkaline hydrogen evolution reaction (HER) performance of the synthesized amorphous Ni–Co–S–O-based electrocatalysts, with varying Ni–Co ratios, was evaluated using a standard three-electrode system in a 1 M aqueous potassium hydroxide solution (Figure 3). The HER reactivity of the samples was examined using the linear scanning voltammetry (LSV) test. As shown in Figure 3a, the amorphous 3Ni–Co–S–O sample demonstrated superior alkaline HER activity, necessitating overpotentials of merely 104, 142, and 170 mV to reach the HER current densities of 100, 500, and 1000 mA cm^{−2}, respectively. Impressively, this HER activity outperformed those of the samples with different Ni–Co ratios and even exceeded the performance of the commercial Pt/C electrocatalyst, which required 105, 152, and 188 mV to achieve the corresponding HER current densities. We also present uncompensated LSV curves that correspond to Figure 3a, as depicted in Figure S4 (Supporting Information), to showcase the actual HER activity of the catalysts. The results indicate that the amorphous 3Ni–Co–S–O maintains optimal alkaline HER performance when uncompensated. The mass loading of a catalyst typically influences its catalytic performance. Our test

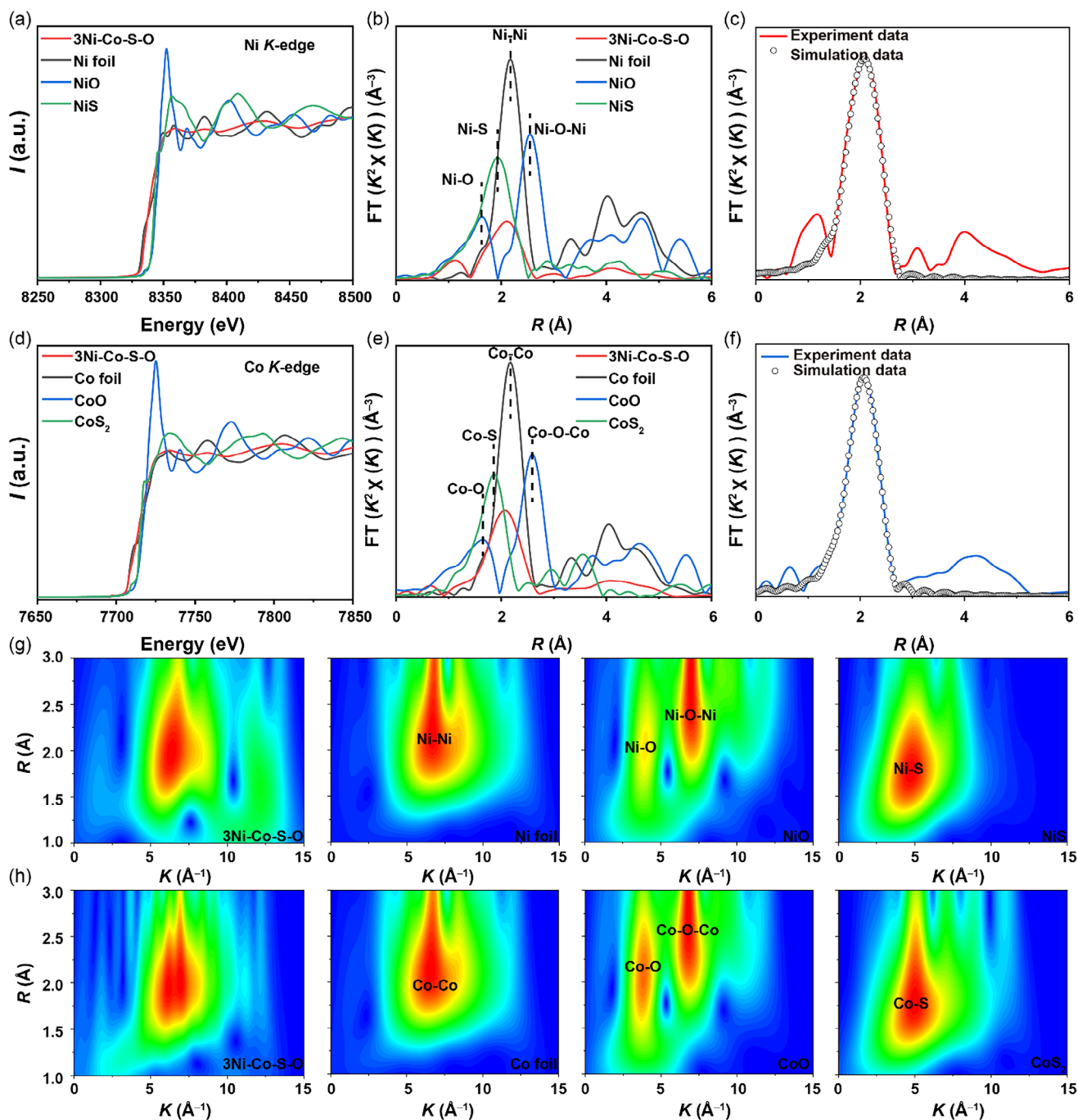


Figure 2. XAS characterizations. a) The Ni K-edge XANES spectra, b) Fourier transforms of Ni K-edge EXAFS spectra, c) Ni K-edge EXAFS analysis in R space, and g) the small wavelet transformation of the 3Ni-Co-S-O, Ni foil, NiO, and NiS samples. d) The Co K-edge XANES spectra, e) Fourier transforms of Co K-edge EXAFS spectra, f) Co K-edge EXAFS analysis in R space, and h) the small wavelet transformation of the 3Ni-Co-S-O, Co foil, CoO, and CoS₂ samples.

results (Table S3, Supporting Information) demonstrated that the variance in mass loading among the xNi-Co-S-O samples, with varying Ni-Co ratios and a fixed deposition time of 40 min, was minimal. This suggests that the contrast in HER performance among these samples stemmed more from their intrinsic activity than from mass loading. To delve deeper into the rela-

tionship between mass loading and HER activity, we prepared 3Ni-Co-S-O samples with deposition times ranging from 10 to 50 min. The LSV test results revealed that an increase in deposition time from 10 to 40 min corresponded with an increase in both the samples' mass loading and their HER activity. However, further extending the deposition time to 50 min led to a

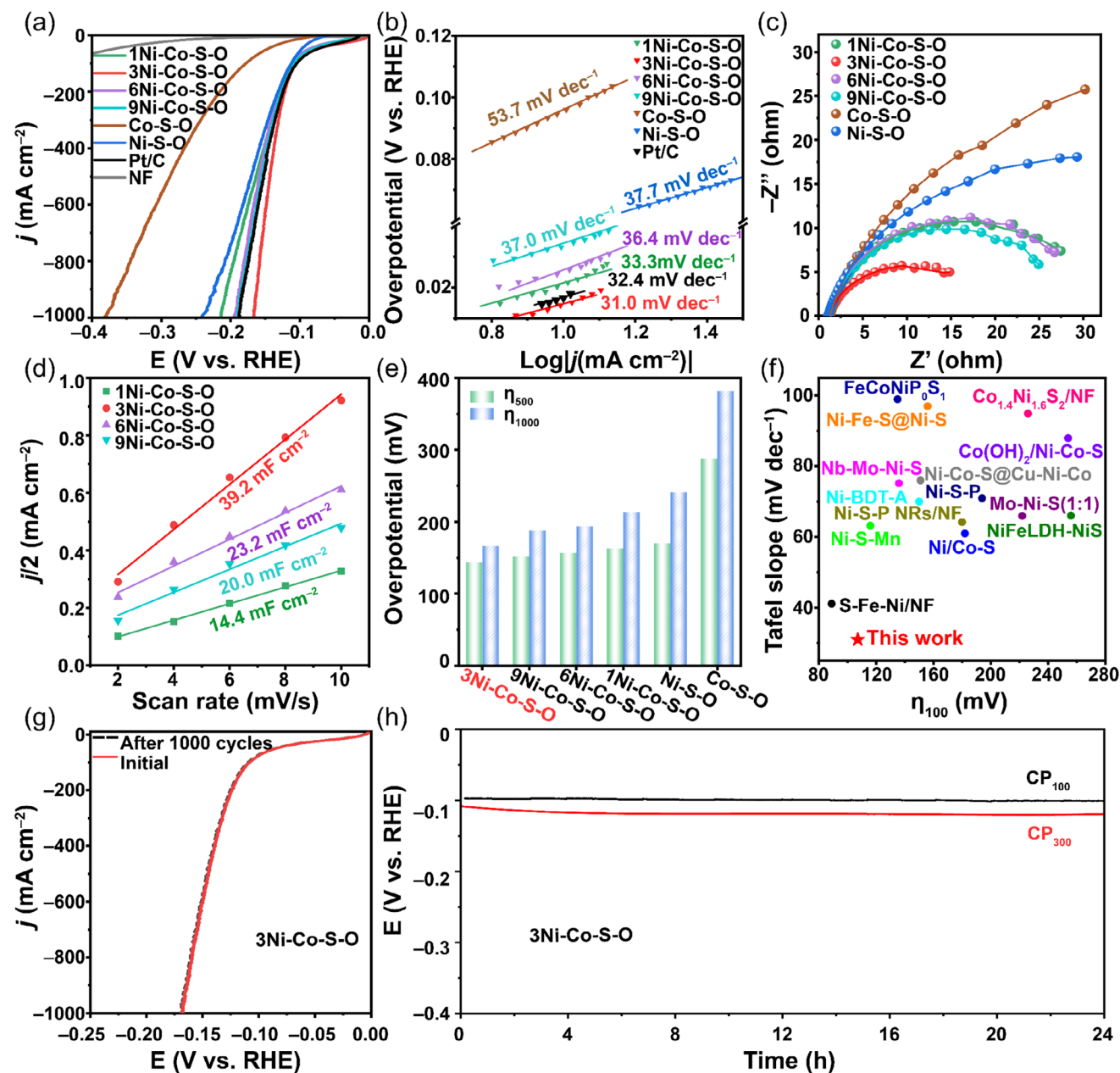


Figure 3. HER performance in 1 KOH. a) LSV curves. b) Tafel plots. c) EIS Nyquist plots. d) Calculated C_{dl} . e) Comparison of overpotentials at HER current densities of 500 and 1000 mA cm⁻². f) Comparison of the overpotentials and Tafel slopes for the best-performed amorphous 3Ni-Co-S-O sample and some recently reported Ni-based electrocatalysts.^[26] g) LSV curves of the amorphous 3Ni-Co-S-O catalyst before and after 1000 CV cycles. h) Chronopotentiometry curves of the amorphous 3Ni-Co-S-O catalyst at HER current densities of 100 and 300 mA cm⁻² for a duration of 24 h.

decrease in HER activity, despite a continued increase in mass loading (Figure S5, Supporting Information). This could be attributed to the fact that excessively long deposition times result in increased thickness and a subsequent decrease in the electron transport properties of the material, thereby negatively impacting its high-potential catalytic performance. EIS results reinforced this observation, demonstrating that the sample with a deposition time of 50 min exhibited higher charge-transfer resistance (Figure S5b and Table S4, Supporting Information), thus confirming a reduction in the material's electrical conductivity.

Therefore, we selected 40 min as the optimal deposition time for this study.

The Tafel slope, derived from the linear relationship between the logarithm of current density and overpotential, is a critical parameter for evaluating the reaction kinetics in the HER process. A smaller Tafel slope signifies a lesser change in overpotential with an increase in reaction current density, indicative of faster electrocatalytic reaction kinetics. To further examine the HER kinetics of the amorphous Ni-Co-S-O samples, we extrapolated the Tafel plots from the corresponding LSV curves to determine their

Tafel slopes (Figure 3b). The results reveal that the amorphous 3Ni–Co–S–O sample presents a Tafel slope of 31.0 mV dec⁻¹, significantly lower than those of the 1Ni–Co–S–O (33.3 mV dec⁻¹), 6Ni–Co–S–O (36.4 mV dec⁻¹), 9Ni–Co–S–O (37.0 mV dec⁻¹), Co–S–O (53.7 mV dec⁻¹), and Ni–S–O (37.7 mV dec⁻¹) samples. Figure S6 (Supporting Information) depicts the Tafel slope, deduced from the analysis of LSV curves at high current densities, providing further insight into the reaction kinetics of the catalyst under these conditions. The findings indicate that the 3Ni–Co–S–O samples also present low Tafel slopes in the region of high current density. These findings in Tafel slopes underscore the superior electrolytic HER kinetics of the amorphous 3Ni–Co–S–O sample in alkaline electrolyte. The catalyst's Tafel slope also relates to the HER mechanism. The calculated Tafel slope of 31.0 mV dec⁻¹ for the amorphous 3Ni–Co–S–O catalyst in this study suggests a two-electron transfer process following a Volmer-Tafel mechanism of bimolecular adsorption and hydrogen evolution, with a theoretical Tafel slope of 30 mV dec⁻¹.^[27] To examine the charge-transfer behaviors during the interfacial HER process between catalysts and electrolytes, we conducted an analysis of the electrochemical impedance spectroscopy (EIS) Nyquist plots for Ni–Co–S–O-based samples, as shown in Figure 3c. The fitted results from the EIS data are included in Table S5 (Supporting Information). Our findings reveal that the prepared Ni–Co–S–O-based samples maintain a similar series resistance (R_s , predominantly determined by the solution resistance between the electrodes), but display significant variations in charge-transfer resistance (R_{ct}). This variation underscores the differing electrocatalytic activity across the investigated samples. Notably, the amorphous 3Ni–Co–S–O sample exhibits the lowest R_{ct} value, suggesting its superior electron transfer rate compared to the other samples.

The study of the double layer capacitance (C_{dl}) of catalysts sheds light on the superior HER activity exhibited by the amorphous 3Ni–Co–S–O sample; this is because C_{dl} is directly proportional to the electrochemically active surface area (ECSA).^[28] Cyclic voltammetry (CV) curves (Figure S7, Supporting Information) were evaluated within non-Faraday potential intervals at various sweep speeds (2, 4, 6, 8, and 10 mV s⁻¹), from which electrochemical C_{dl} values were deduced (Figure 3d). The computed C_{dl} values for the 1Ni–Co–S–O, 3Ni–Co–S–O, 6Ni–Co–S–O, and 9Ni–Co–S–O samples were 14.4, 39.2, 23.2, and 20.0 mF cm⁻², respectively. Notably, the 3Ni–Co–S–O sample yielded the highest C_{dl} value, suggesting a greater number of catalytically active sites, a finding that aligns with its exceptional alkaline HER performance. The turnover frequency (TOF), defined as the number of molecules produced per second per active site, serves as a crucial parameter for evaluating the intrinsic activity of a catalyst.^[29] Thus, we examined the TOFs of the synthesized Ni–Co–S–O-based catalysts. To quantify the active sites and calculate the TOF values, we initially conducted CV tests in a 1 M phosphate buffer solution (PBS).^[30] Utilizing the CV data and specific equations (provided in the Experimental section), we then got the TOF values (Figure S8, Supporting Information). At an overpotential of 150 mV (vs RHE), the 3Ni–Co–S–O catalyst exhibited the highest TOF value of 0.553 s⁻¹, indicating superior intrinsic catalytic activity.

To intuitively illustrate the exceptional alkaline HER reactivity of the synthesized amorphous 3Ni–Co–S–O catalyst, we com-

pared the overpotentials required to achieve HER current densities of 500 and 1000 mA cm⁻² (η_{500} and η_{1000}) across the range of prepared Ni–Co–S–O-based materials. Additionally, we contrasted the η_{100} and Tafel slopes of the best-performing amorphous 3Ni–Co–S–O catalyst with those of other recently reported Ni–S-based HER electrocatalysts (Figure 3f; Table S6, Supporting Information).^[26] The results clearly indicate that the amorphous 3Ni–Co–S–O catalyst outperforms these electrocatalysts in terms of HER performance.

The durability of a catalyst's HER is a crucial criterion for evaluating its suitability for practical implementation. This is particularly significant for amorphous catalysts, as current leading-edge amorphous catalysts frequently exhibit unsatisfactory stability.^[15] As such, the electrochemical HER stability of the highest-performing amorphous 3Ni–Co–S–O was assessed using cyclic voltammetry (CV) cycles and chronopotentiometry (CP) in 1 M KOH (Figure 3g,h). The LSV curves of the amorphous 3Ni–Co–S–O catalyst, before and after 1000 CV cycles, nearly overlap (Figure 3g). In the CP test, the amorphous 3Ni–Co–S–O catalyst maintained stable operation for 24 h at HER current densities of 100 and 300 mA cm⁻², with only 2 and 15 mV increases in overpotentials, respectively (Figure 3h). To further validate the catalyst's stability over an extended duration, we augmented the stability test with a more protracted timeframe, illustrated in Figure S9 (Supporting Information). The findings indicate that the 3Ni–Co–S–O catalyst maintains stable operation for 85 h at a current density of 100 mA cm⁻². These CV and CP test outcomes demonstrate that the synthesized amorphous 3Ni–Co–S–O catalyst possesses exceptional electrocatalytic alkaline HER stability under high current densities, suggesting its potential for industrial applications.

2.3. Observation of Surface Gradient Layer

The notable stability of the alkaline HER prompts an examination of the structural stability of the amorphous 3Ni–Co–S–O material post-HER process, given that the catalyst's structure significantly influences its catalytic performance. Consequently, we conducted structural characterizations (XRD, SEM, and TEM) on the 3Ni–Co–S–O sample following the HER CP test at 300 mA cm⁻² for 24 h (Figure 4). The XRD results in Figure 4a reveal that the 3Ni–Co–S–O sample retains its original amorphous nature post-HER CP test, with no observable crystal phase. SEM observations (Figure 4b,c) and SEM-coupled EDS-mapping results (Figure S10a–c, Supporting Information) indicate minimal morphological changes in the 3Ni–Co–S–O catalyst after the HER CP test, preserving its nanostructure. The TEM and HRTEM images and SAED pattern in Figure 4d–f show no evidence of crystal lattice information, confirming that the 3Ni–Co–S–O catalyst maintains its original amorphous characteristic post-HER CP test, without any phase transition or crystal growth. The HAADF-STEM image and corresponding EDS mapping results in Figure 4g reveal a uniform Ni, Co, S, and O elemental distribution in the 3Ni–Co–S–O catalyst, further affirming the relative stability of the amorphous structure.

Despite the 3Ni–Co–S–O sample retaining its amorphous structure after the HER process (CP₃₀₀ for 24 h), there is a notable change in its chemical composition. Initially, the composition is

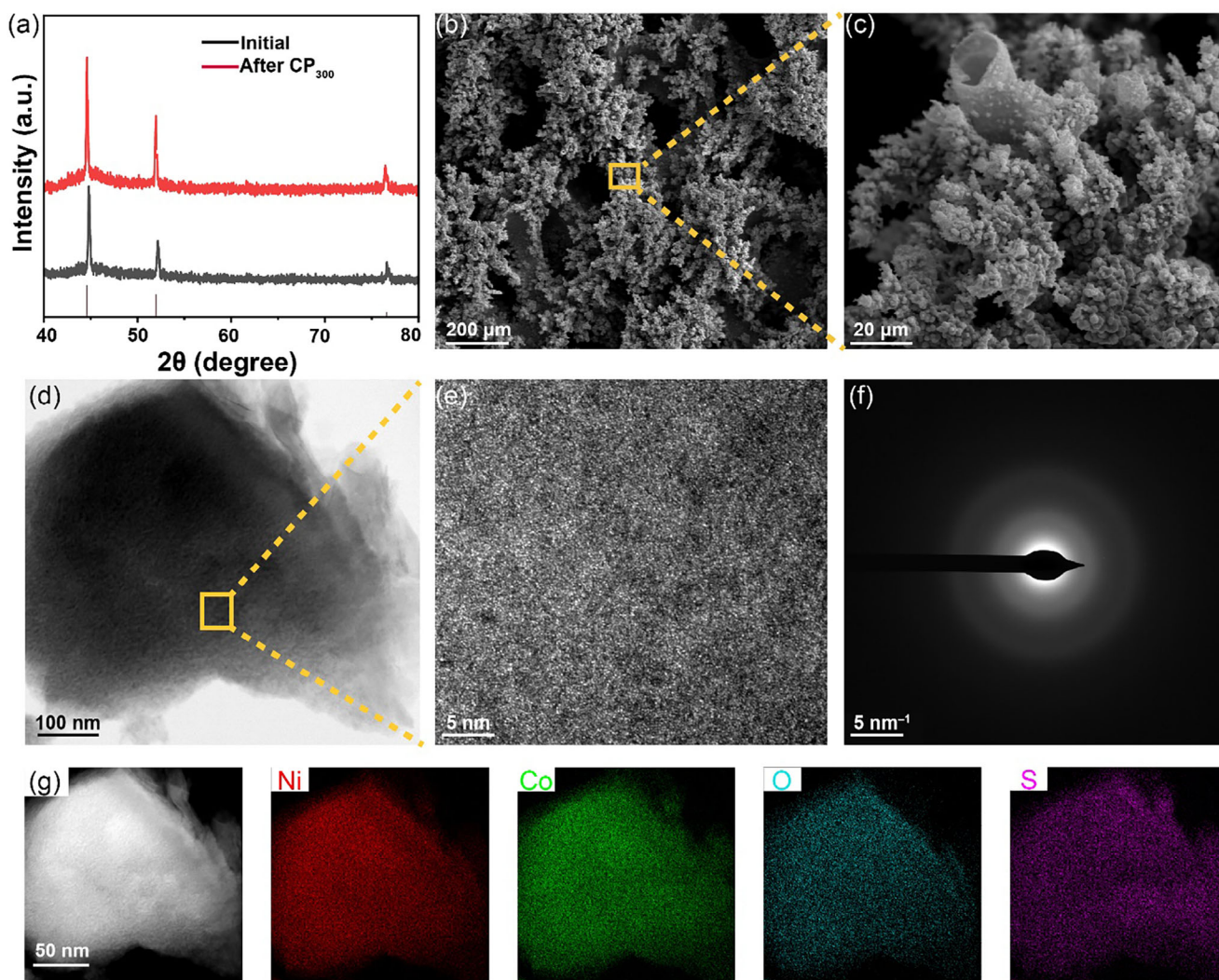


Figure 4. Structure stability evolution of the amorphous 3Ni–Co–S–O material after the HER process. a) XRD patterns. b,c) SEM images. d) TEM image. e) HRTEM image. f) SAED pattern. g) HAADF-STEM image and corresponding EDS mapping results.

$\text{Ni}_{5.3}\text{Co}_{1.4}\text{S}_{1.2}\text{O}_1$, which transforms to $\text{Ni}_{3.8}\text{Co}_{0.4}\text{S}_{0.6}\text{O}_1$ (Table S1, Supporting Information) post-process. This observation prompts further investigation into the surface compositional and structural evolution of the 3Ni–Co–S–O sample during HER. It is crucial to note that the catalyst's surface plays a direct role in the HER reaction. To elucidate this transformation, we employed characterization techniques such as SEM, EDS, Raman, and XPS on the 3Ni–Co–S–O sample, both before and after undergoing CP₃₀₀ for 24 h (Figure 5). In Figure 5a,b, it is evident that the four elements of Ni, Co, S, and O are uniformly distributed across the section of the 3Ni–Co–S–O catalyst prior to the HER test. However, post-HER test, the distribution of these elements alters. As depicted in Figure 5c,d, when moving toward the catalyst's surface at a depth of $\approx 6 \mu\text{m}$, the content of Ni and S elements progressively decreases. Concurrently, the O element's content incrementally increases, while the Co element's content remains largely consistent. During the HER process, water molecules undergo decomposition into OH^- and H_2 . Subsequently, the OH^- ions and adsorbed O_2 participate in the surface reconstruction of

the catalyst, leading to a marked enhancement in the oxygen content on the catalyst. The insights from the SEM-coupled EDS line-scan indicate that the amorphous 3Ni–Co–S–O catalyst undergoes a surface reconstruction phase, leading to the formation of a gradient layer on its surface post-HER process. We conducted further tests to examine the surface morphology and compositional changes of the 3Ni–Co–S–O sample after a 24 h immersion in 1 M KOH electrolyte without HER reaction (Figures S10d–f and S11, Supporting Information). The results reveal that the sample's morphology remains consistent and its cross-sectional elemental distribution is uniform. No surface reconstruction phenomenon was observed. This finding suggests that the surface reconstruction process of the catalyst solely occurs during the HER process, thereby reinforcing the critical role of the electrochemical HER reaction in the surface reconstruction process.

The Raman spectroscopy data elucidate the changes in the chemical structure of the amorphous 3Ni–Co–S–O sample before and after the HER process (Figure 5e). It is evident that the initial 3Ni–Co–S–O sample primarily exhibits the

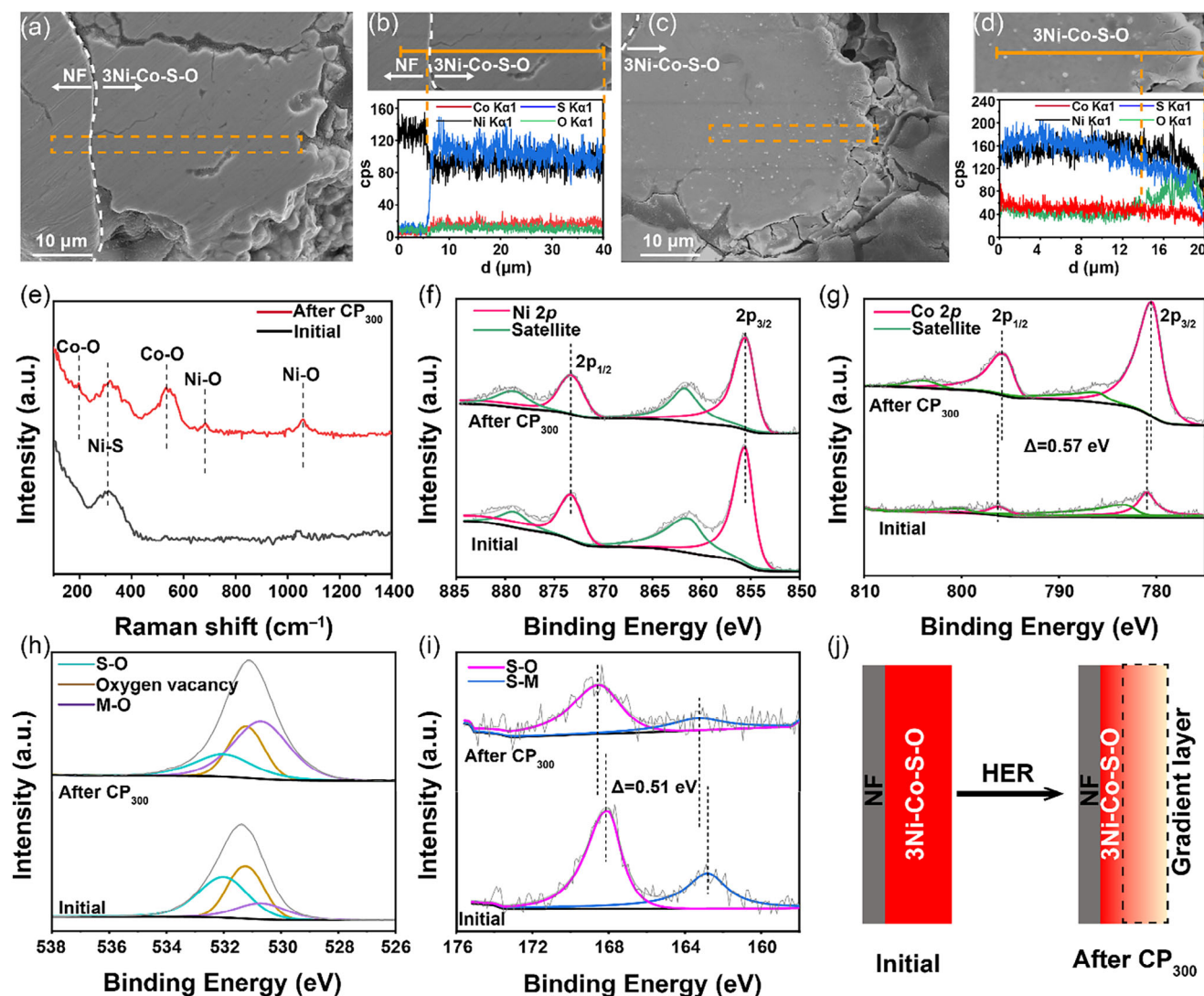


Figure 5. Surface reconstruction and functional gradient layer formation on the amorphous 3Ni-Co-S-O catalyst after the HER process. a) SEM and b) EDS line-scan of a cross-section for the 3Ni-Co-S-O sample before HER. c) SEM and d) EDS line-scan of a cross-section for the 3Ni-Co-S-O sample after HER (CP₃₀₀ for 24 h). e) Raman spectra and XPS spectra of f) Ni 2p, g) Co 2p, h) O 1s, and i) S 2p orbitals of the 3Ni-Co-S-O sample before and after HER (CP₃₀₀ for 24 h). j) A schematic of the surface reconstruction and surface gradient layer formation during the HER process.

vibrational modes of Ni-S at 311 cm⁻¹. Post-HER, there is a notable decrease in the intensity of this Ni-S Raman signal, which can be attributed to the dissolution of the sulfur element in the restructured surface layer. Interestingly, new vibrational modes emerge for Co-O at 197 and 532 cm⁻¹, and for Ni-O at 683 and 1059 cm⁻¹. These are indicative of an increased oxygen content in the gradient surface layer formed after reconstruction.

To further investigate the reconstruction phenomenon on the material surface, XPS characterizations were employed to analyze the chemical information pertaining to the surface elemental chemical states of the 3Ni-Co-S-O catalysts both pre and post-HER process (Figure 5f-i). As depicted in Figure 5f, the Ni 2p XPS spectra of the 3Ni-Co-S-O catalysts prior to HER are segmented into four distinct peaks. The two peaks manifested at 855.49 and 873.13 eV correspond to the Ni 2p_{3/2} and Ni 2p_{1/2}

orbitals respectively, while the remaining two peaks at 861.73 and 879.01 eV represent satellite peaks. After HER, no observable peak shifts occur for these four orbitals; however, a reduction in peak intensity is evident. This could potentially be attributed to the partial dissolution of the Ni element during HER, a hypothesis supported by the SEM-coupled EDS line-scan results presented in Figure 5d. In parallel with the Ni 2p spectra, the Co 2p XPS spectra of the 3Ni-Co-S-O catalysts preceding HER are divided into four peaks: two associated with the Co 2p_{3/2} and Co 2p_{1/2} orbitals and two more representing satellite peaks (Figure 5g). Interestingly, post-HER, there is a notable increase in the intensity of these four peaks. We speculate that the dissolution of Ni and S elements results in the exposure of the Co element, thereby leading to an increase in the intensity of the Co 2p XPS orbital. Moreover, it is worth mentioning that after HER, the peaks exhibit a shift toward lower binding energies,

suggesting a reduced valance state for the Co element relative to its state pre-HER.

In Figure 5h, the O 1s XPS spectra of the 3Ni–Co–S–O catalyst prior to HER are delineated into three distinct peaks: S–O (at 532.00 eV), M–O (at 530.69 eV), and oxygen vacancies (at 531.21 eV). Post-HER, there is a marked augmentation in the intensity of the O 1s XPS peak, attributed to the elevated O content within the reconstructed gradient surface layer. It's observed that the oxygen vacancy peak remains consistent post-HER. However, the S–O peak's intensity diminishes, while that of the M–O peak amplifies. This can be attributed to the reduced concentration of the S element and the augmented proportion of the O element within the reconstructed gradient surface layer. In Figure 5i, the S 2p XPS spectra of the 3Ni–Co–S–O catalyst pre-HER are segmented into two peaks, labeled S–O (at 168.04 eV) and S–M (at 162.78 eV). After HER, a significant decline in the intensity of these peaks is evident, indicative of the S element's dissolution in the reconstructed gradient surface layer. A notable positive shift in the binding energies of the S orbitals post-HER is also observed. This shift results from the increased oxygen incorporation post-HER, leading to a reduced binding strength between S and other elements, given the lower electronegativity of S compared to the O element.

The elemental and structural analyses of the catalyst reveal that following the HER process, a self-optimizing surface reconstruction transpires on the amorphous 3Ni–Co–S–O catalyst's surface. This results in the formation of a functional gradient layer, which is accountable for its enduring HER activity and stability.

The process of surface reconstruction of catalysts during electrochemical reactions is intricate and vital. Previous studies have also examined the surface reconstruction of these catalysts. For instance, the enhanced performance of the c-Ni₂P₄O₁₂/a-NiMoOx/NF catalyst, as developed by Wang et al.,^[31] was primarily due to the surface re-construction initiated by HER. This was further characterized by the dissolution of the passivation layer, the emergence of activation following the initial CV cycle, and the establishment of stable surface components after 200 cycles. Moreover, the HER efficacy of Ni–S coordination polymer 2D nanosheets, synthesized by Hu et al.,^[26m] witnessed a significant enhancement post-1000 electrochemical activations. Notably, their thickness reduced from 16 to 1.4 nm, the sulfur content declined to 2.7%, while the oxygen content surged to 67.0%. These findings suggest that Ni⁰ serves as the primary active site, with the synergistic interplay between S and Ni being instrumental in modulating HER activity. Such research offers valuable insights for our comprehension of the surface reconstruction processes in 3Ni–Co–S–O catalysts.

We further investigate the formation process of surface reconstruction and its subsequent impact on catalyst performance, specifically focusing on the best-performed 3Ni–Co–S–O catalyst. The analysis includes a comparison of the catalyst's HER performance, electrochemical impedance, and cross-sectional elemental distribution, as well as its chemical state before and after 100 cycles of CV activation. As illustrated in Figure S12 (Supporting Information), there is a significant increase in the catalyst's HER performance after the activation process, with a corresponding decrease in R_s and R_{ct} values. The reduction in R_s suggests an improvement in the internal resistance of the electrode material and the interface contact resistance between the electrolyte

and the electrode. Meanwhile, the decrease in R_{ct} signifies an enhancement in charge-transfer dynamics on the catalyst surface. Further examination through cross-sectional EDS line-scan analysis (Figure S13, Supporting Information) reveals that Ni, Co, S, and O elements in the sample are evenly distributed before the CV activation. However, after activation, these elements exhibit a clear gradient distribution in the vertical direction, with the gradient layer thickness closely resembling that after the CP₃₀₀-24 h test in Figure 5d. Taken together, these findings indicate that the 3Ni–Co–S–O catalyst undergoes surface reconstruction during the CV activation, leading to optimizations in its electron transport properties and HER catalytic activity.

To elucidate the alterations in composition and chemical state of the gradient layer after CV activation, XPS depth etching experiments were performed (Figure 6). Prior to CV activation, the valence states and contents of Ni, Co, and S remained consistent from the surface to the inside (Figure 6a–c). However, after CV activation, distinct changes were observed. As the etching depth increased, the peak intensity for Ni 2p XPS spectra intensified but its binding energy remained constant, suggesting a gradual increase in its elemental content from the surface to the inside (Figure 6d). For Co, there was no variation in peak strength or binding energy post-activation, indicating that both its elemental content and valence state remained stable (Figure 6e). In the case of S 2p XPS spectra, post-activation, the intensity of the S–O bond diminished with a reduction in O content, while the S–M (M=Ni, Co) bond intensity grew. The entire spectrum peak shifted toward lower binding energy, suggesting a decrease in the valence state of S (Figure 6f). These observations align with the cross-sectional line scanning EDS and surface XPS data of CP₃₀₀ after 24 h, collectively confirming the surface reconstruction of elemental composition and chemical state during the CV activation process.

Leveraging the benefits of density functional theory (DFT) for a comprehensive understanding of the electronic structure and reaction mechanisms of catalysts, we then employed DFT calculations to investigate the impact and mechanism of gradient amorphous layer formation due to surface reconstruction on the performance of HER catalysts. We analyzed the alkaline HER reaction process and the associated energy barriers for four catalytic systems: 3Ni–Co–S–O, reconstructed 3Ni–Co–S–O, Ni–S–O, and Co–S–O (Figure 7; Figure S14 and Table S7, Supporting Information). The alkaline HER reaction is often limited by its first step, water dissociation, which presents a high energy barrier and is thus typically the rate-determining step. Through comparative research, we have determined that the metal atoms within these catalysts serve as the active sites for HER catalytic reactions. In both 3Ni–Co–S–O and the restructured 3Ni–Co–S–O catalysts, it was observed that the Co atom sites demonstrate superior HER reaction activity (Figure S14, Supporting Information). Our calculations reveal that the water dissociation energy barriers for the metal active sites on the planes of 3Ni–Co–S–O, Ni–S–O, and Co–S–O are 0.96, 1.59, and 1.69 eV, respectively. Notably, the reconstructed 3Ni–Co–S–O substantially lowers the water dissociation energy barrier to just 0.59 eV (Figure 7e), suggesting its superior thermodynamic efficiency for water dissociation.

Given that the ΔG_{H_2O} description fails to fully encapsulate the comprehensive kinetic process of alkaline HER, we

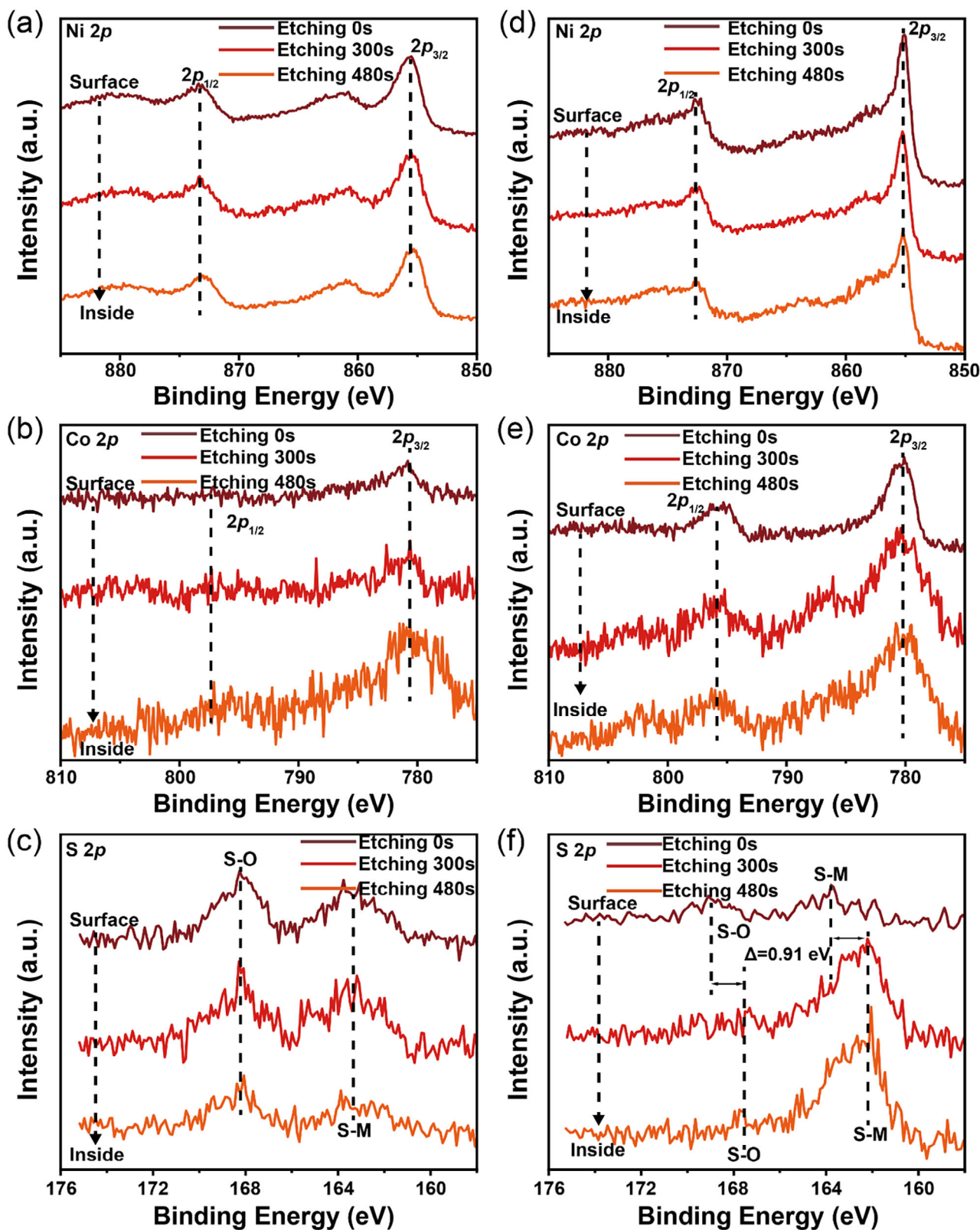


Figure 6. Analysis of the chemical states of elements from the surface to inside (with different etching times). XPS spectra of Ni 2p, Co 2p, and S 2p orbitals of the 3Ni-Co-S-O samples a-c) before and d-f) after CV activation.

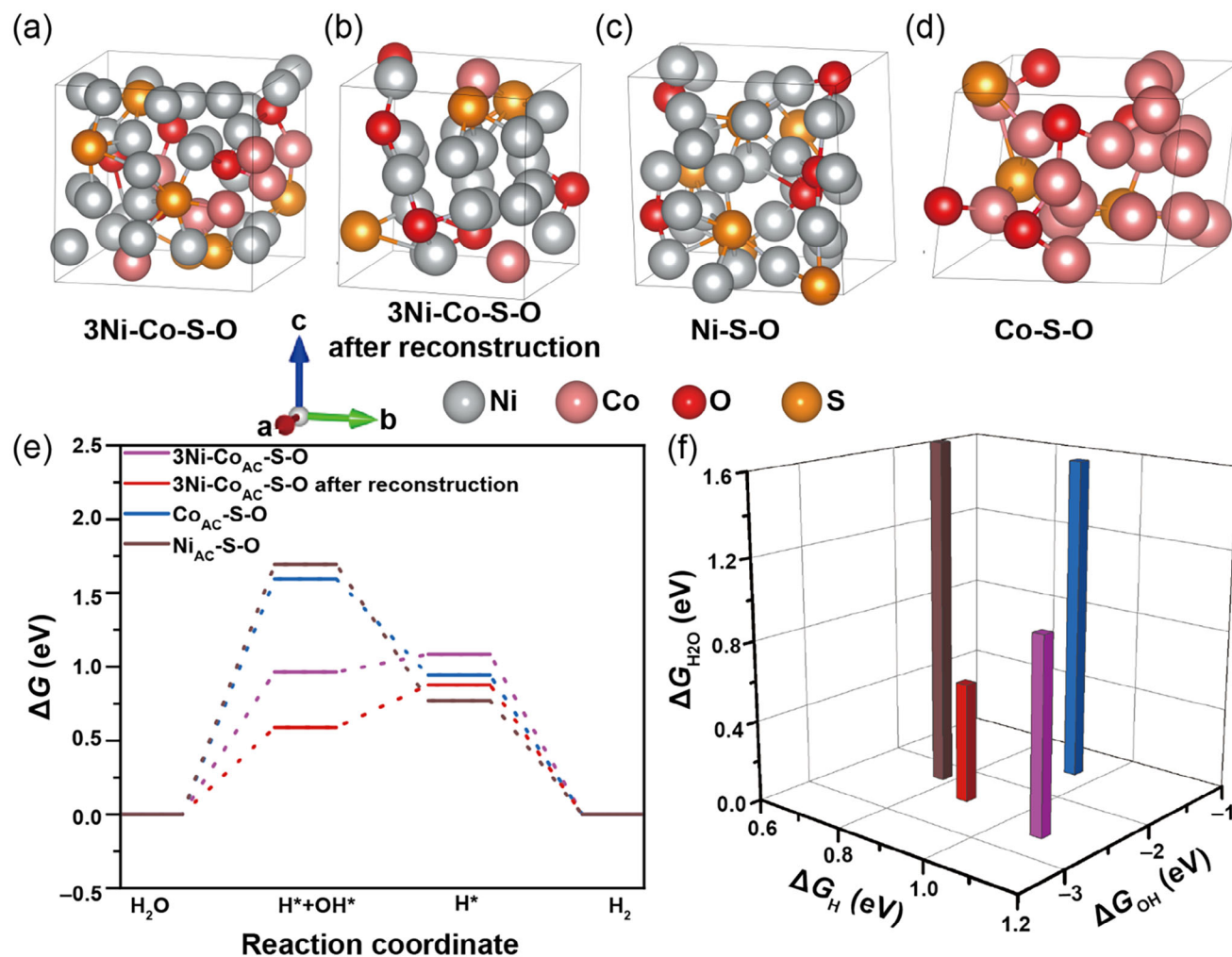


Figure 7. DFT calculations. a–d) Atomic structure of the optimized four amorphous samples. e) Calculated free energy diagram of HER for four samples (AC means active site). f) Comparison of the energy barriers of water dissociation (ΔG_{H_2O} , the Volmer step) and intermediate hydrogen adsorption (ΔG_H , the Tafel or Heyrovsky step) and chemisorption energies of hydroxyl (ΔG_{OH}) for the four samples during HER.

additionally present two crucial descriptions: ΔG_H and ΔG_{OH} . ΔG_H serves to delineate the adsorption/desorption capability of H^* intermediates following hydrolytic dissociation, whereas ΔG_{OH} mirrors the chemical adsorption strength of OH^- . As illustrated in Figure 7f and Table S7 (Supporting Information), the reconstructed 3Ni–Co–S–O's ΔG_H value is 0.877 eV, lower than those of Ni–S–O and Co–S–O catalysts. This suggests more efficient H_2 generation kinetics post-hydrolysis dissociation for the reconstructed 3Ni–Co–S–O. Concurrently, its ΔG_{OH} value stands at -2.464 eV, a moderate level, suggesting that the material has struck an optimal balance between fostering hydrolytic dissociation and preventing the hydroxyl (OH^*) adsorption from obstructing active sites. Consolidating these theoretical calculation findings, the intrinsic activity of the four materials in the alkaline HER process can be ranked as follows: reconstructed 3Ni–Co–S–O > 3Ni–Co–S–O > Ni–S–O > Co–S–O. Notably, this ranking aligns with our experimental results, offering significant theoretical underpinning for a profound comprehension of the surface reconstruction process and the mechanism responsible for the enhancement in HER performance.

3. Conclusion

In summary, we have successfully synthesized an amorphous 3Ni–Co–S–O catalyst using a simple electrodeposition method and validated its effectiveness for efficient alkaline HER. Our findings reveal that the material's amorphous nature is well-preserved during the HER process. Interestingly, we observed a surface reconstruction phenomenon wherein the primary elements undergo a self-optimization process, creating a functional gradient surface layer ≈ 6 μm thick. This layer supports long-term active and stable alkaline HER. Significantly, the amorphous 3Ni–Co–S–O electrocatalyst exhibited superior HER activity, with a remarkably low overpotential of just 170 mV to achieve an industrial HER current density of 1000 $mA\ cm^{-2}$, surpassing that of the commercial Pt/C catalyst. Its exceptional alkaline HER activity and stability indicate its high potential for practical application. We attribute the excellent HER performance to the 3Ni–Co–S–O catalyst's amorphous nature and the self-optimization process, which forms a functional gradient layer. We also employ theoretical calculations to elucidate the HER

process and identify the mechanism responsible for enhancing the HER properties of the functional gradient layer on the reconstructed 3Ni–Co–S–O catalyst. Our findings suggest that this layer yields a high density of electrochemically active and stable Co sites. These sites exhibit a low energy barrier for alkaline HER and facilitate rapid reaction kinetics. Our research offers new perspectives on the development of highly efficient alkaline HER electrocatalysts. By altering the chemical composition of the electrolyte for electrodeposition, it is possible to produce a variety of functional materials with even more impressive catalytic performance. Most importantly, our work contributes to the understanding of the high-performance of amorphous electrocatalysts, paving the way for the development of next-generation catalysts.

4. Experimental Section

Chemicals: Nickel foams (0.5 mm-thick), NiSO₄·6H₂O (≥98.5%), and CoSO₄·7H₂O (≥99%) were purchased from Aladdin. NaCl (≥99.5%), CH₄N₂S (≥99%), H₃BO₃ (≥99.8%), C₁₂H₂₅NaO₄S (≥90%), KOH (≥85%), HCl (36–38 wt.%), and acetone (≥99.5%) were purchased from Sinopharm Group. All reagents were directly used without further purification.

The nickel foam underwent a pretreatment process involving HCl (2.0 M), acetone, deionized water, and ethanol, each for a duration of 20 min, under ultrasonic conditions to remove contaminants and surface oxides. Subsequently, the treated nickel foam was preserved in anhydrous ethanol prior to electrodeposition.

Preparation of Amorphous Ni–Co–S–O Electrocatalysts: The amorphous Ni–Co–S–O electrocatalysts were synthesized via electrodeposition on Ni foams. Initially, an electrodeposition solution was prepared by adding CH₄N₂S (1.3 M) and H₃BO₃ (0.65 M) to 200 mL of deionized water. Subsequently, NiSO₄·6H₂O (ranging from 0.30 to 0.49 M) and CoSO₄·7H₂O (from 0.26–0.05 M) were incorporated into the solution under continuous stirring, yielding various Ni–Co ratios (9:1, 6:1, 3:1, and 1:1). Electrodeposition was carried out using an electrochemical workstation (Autolab AUT88436) with a standard three-electrode system: the pretreated nickel foam (2 cm × 1.5 cm) served as the working electrode, an Hg/HgO electrode was used as the reference, and a high-purity graphite rod (99.995%, Sigma–Aldrich) functioned as the counter electrode. The deposition was executed using a constant-current technique at a current density of –50 mA cm^{–2} over a duration of 40 min. Post-deposition, the samples were rinsed with deionized water, then vacuum-dried in an oven at 50 °C for 3 h. The resultant samples were labeled as xNi–Co–S–O, where “x” denotes the prescribed Ni–Co ratio. For comparative analysis, amorphous Co–S–O and Ni–S–O catalysts were also prepared by omitting NiSO₄·6H₂O and CoSO₄·7H₂O from the electrodeposition solution, respectively, following the identical electrodeposition protocol as the Ni–Co–S–O electrocatalysts.

Material Characterizations: The morphology and nanostructure of the samples were examined using a field emission scanning electron microscope (FE-SEM, Hitachi Regulus8100) and a transmission electron microscope (TEM, FEI Talos-F200S). The phase crystallinity of the catalysts was assessed by an X-ray diffractometer (Rigaku Smart Labs), employing Cu K α radiation ($\lambda = 1.5418 \text{ \AA}$). Raman spectra were gathered using a Raman spectrometer (HORIBA HR Evolution) with a 532 nm laser to determine the chemical bonding properties of the samples. Elemental compositions were derived from energy-dispersive X-ray spectrometers integrated with the SEM and TEM instruments. X-ray photoelectron spectroscopy (XPS, Thermo Fisher Scientific K-Alpha) was utilized to ascertain elemental compositions and valence states. Ni K-edge and Co K-edge analysis were performed with Si (111) crystal monochromators at BL 14W1 beamlines, at the Shanghai Synchrotron Radiation Facility (SSRF) (Shanghai, China). The electrodeposited samples were carefully scraped off the nickel foam

surface and collected for the XAS test. Before the analysis at the beamline, samples were pressed into thin sheets with 1 cm in diameter and sealed using Kapton tape film. Ni K-edge and Co K-edge EXAFS and XANES spectra of the 3Ni–Co–S–O sample and standard samples (including Ni metal, NiS, NiO, Co metal, CoS₂, and CoO) were recorded in transmission mode. The XAS data were processed and analyzed by the software codes Athena and Artemis.

Electrochemical Measurement: Electrochemical performance tests were conducted on the synthesized catalysts, encompassing electrochemical hydrogen evolution testing and stability assessments. These evaluations were executed using an electrochemical workstation (Autolab AUT88436) within a standard three-electrode system, employing a 1 M KOH solution as the electrolyte. The working electrode, which consisted of the synthesized catalyst, measured 1 cm × 1 cm in the electrolyte. A high-purity graphite rod (99.995%, Sigma–Aldrich) was used as the counter electrode, and a Hg/HgO electrode served as the reference. All experiments were conducted at room-temperature. Potentials were calibrated to a reversible hydrogen electrode (RHE) using relations of $E(\text{RHE}) = E(\text{Hg}/\text{HgO}) + 0.925 \text{ V}$. The electrochemical hydrogen evolution tests included linear sweep voltammetry (LSV) and electrochemical impedance spectroscopy (EIS). Prior to conducting the LSV test, a cyclic voltammetry (CV) activation process consisting of 100 cycles was carried out at a rate of 50 mV s^{–1}. During LSV measurements, a forward scan was conducted at a rate of 5 mV s^{–1} across a potential range of 0.05 to –0.8 V. EIS was performed at open circuit potential ($\approx -0.2 \text{ V}$ vs RHE) with an AC voltage amplitude of 5 mV, covering a frequency range from 0.01 Hz to 100 kHz. HER stability tests included CV cycling and chronoamperometry (CA) test. For the CV cycling test, the working electrode (the synthesized catalyst) was subjected to 1000 continuous cycles in a 1 M KOH solution at a scan rate of 50 mV s^{–1}, followed by LSV analysis of the cyclic voltammogram. For the CP assessment, continuous operation for 24 h in 1 M KOH solution was conducted at current densities of –100 and –300 mA cm^{–2}. Electrochemical stability was evaluated by comparing the LSV behaviors before and after CV cycling, as well as the CA responses at appropriate potentials.

Calculations of C_{dl} : The double layer capacitance (C_{dl}) was determined from the CV curves in a non-Faradaic potential range (selected as 0.2 to 0.3 V vs RHE in this work). Because the CV curves were quite rectangular, the C_{dl} values could be estimated by plotting the ΔJ ($J_{anodic} - J_{cathodic}$) at 0.25 V versus RHE against the scan rates (2, 4, 6, 8, and 10 mV s^{–1}), in which the slope is twice of C_{dl} .

TOF Calculations: TOF is calculated by the following Equation (1):

$$\text{TOF} = \frac{J}{2Fn} \quad (1)$$

where J is the cathodic current density ($A = C \text{ s}^{-1}$) for HER at a specific overpotential in 1 M KOH, F is the Faraday constant ($96\,485.4 \text{ C mol}^{-1}$), n is the active number of different electrodes (mol). To quantify the active sites and calculate the TOF values, CV tests were first performed in 1 M phosphate buffer solution (PBS) with voltages ranging from –0.2 to 0.6 V (vs RHE) at a scan rate of 50 mV s^{–1}. By integrating the CV curve, one can determine the charge value (Q). The number of active sites (n) could be estimated as a linear positive correlation with Q for a given geometric area. In this study, the formula $n = Q/(2F)$ was employed, consistent with previous reports.^[30]

DFT Calculations: All DFT calculations were performed using the Perdew–Burke–Ernzerhof (PBE) generalized gradient approximation (GGA)^[32] in the Vienna ab initio Simulation Package (VASP)^[33] with the projector augmented wave (PAW) method^[34] and a plane-wave basis set. van der Waals (vdW) corrections were included via the DFT-D3 method,^[35] and a 20 Å vacuum layer was applied to avoid periodic interactions. Structural relaxations used the conjugate gradient algorithm with a 350 eV plane-wave kinetic energy cutoff, converging to 10^{–6} eV for energy and 0.05 eV Å^{–1} for forces. The amorphous properties were simulated using ab initio molecular dynamics (MD)^[36] with a melt-quench process. Crystalline supercells of initial 3Ni–Co–S–O, 3Ni–Co–S–O after reconstruct, Ni–S–O and Co–S–O were melted at 5000 K for 5 ps to remove

crystallinity, then quenched to 1500 at 700 K ps⁻¹, held for 5 ps, and further quenched to 300 K in 1 ps. The quenched structures were equilibrated at 300 K for 5 ps and optimized geometrically. Simulations used the NVT ensemble with the Nose–Hoover thermostat^[37] and a 1 fs time step. The cooling rate, though faster than experimental rates (1 K s⁻¹), was validated to reproduce experimental atomistic structures effectively.

For the determination of hydroxide ion free energy, the thermodynamic relation: $G(\text{OH}^-) = G(\text{H}_2\text{O}) - G(\text{H}^+)$ was adopted under the equilibrium condition $\text{H}^+ + \text{OH}^- \rightleftharpoons \text{H}_2\text{O}$.^[38] The free energy of protons ($G(\text{H}^+)$) was approximated as half the free energy of molecular hydrogen.^[38] The total thermodynamic free energy was computed using:

$$G = E_{\text{DFT}} + E_{\text{ZPE}} - TS \quad (2)$$

where E_{DFT} denotes the DFT-derived total energy, EZPE was calculated using the following equation:

$$E_{\text{ZPE}} = \frac{1}{2} \sum_i h\nu_i \quad (3)$$

represents the zero-point energy calculated under the harmonic approximation using vibration frequencies (ν) obtained from DFT. Molecular entropies were adopted from established thermochemical tables,^[39] while vibrational entropies for adsorbed species were evaluated through: as implemented in.^[40]

$$S = k_B \left[\sum_i \ln \left(\frac{1}{1 - e^{-h\nu_i/k_B T}} \right) + \sum_i \frac{h\nu_i}{k_B T} \left(\frac{1}{e^{h\nu_i/k_B T} - 1} \right) + 1 \right] \quad (4)$$

Supporting Information

Supporting Information is available from the Wiley Online Library or from the author.

Acknowledgements

This work was financially supported by the Guangdong Major Project of Basic and Applied Basic Research (Grant No. 2021B0301030001) and the General Program of Natural Science Foundation of Jiangsu Province, China (Grant No. BK20221179).

Conflict of Interest

The authors declare no conflict of interest.

Data Availability Statement

The data that support the findings of this study are available from the corresponding author upon reasonable request.

Keywords

alkaline water electrolysis, amorphous catalysts, functional gradient layer, high-performance, surface reconstruction

Received: March 21, 2025

Published online:

- [1] P. Zhou, I. A. Navid, Y. Ma, Y. Xiao, P. Wang, Z. Ye, B. Zhou, K. Sun, Z. Mi, *Nature* **2023**, 613, 66.
- [2] A. Ursua, L. M. Gandia, P. Sanchis, *Proc. IEEE* **2011**, 100, 410.
- [3] R. Subbaraman, D. Tripkovic, D. Strmcnik, K. C. Chang, M. Uchiumura, A. P. Paulikas, V. Stamenkovic, N. M. Markovic, *Science* **2011**, 334, 1256.
- [4] M. Lao, P. Li, Y. Jiang, H. Pan, S. X. Dou, W. Sun, *Nano Energy* **2022**, 98, 107231.
- [5] Y. Zhu, L. Li, H. Cheng, J. Ma, *JACS Au* **2024**, 4, 4639.
- [6] A. A. Feidenhans'l, Y. N. Regmi, C. Wei, D. Xia, J. Kibsgaard, L. A. King, *Chem. Rev.* **2024**, 124, 5617.
- [7] T. Ling, T. Zhang, B. Ge, L. Han, L. Zheng, F. Lin, Z. Xu, W. B. Hu, X. W. Du, K. Davey, *Adv. Mater.* **2019**, 31, 1807771.
- [8] J. Kibsgaard, C. Tsai, K. Chan, J. D. Benck, J. K. Nørskov, F. Abild-Pedersen, T. F. Jaramillo, *Energy Environ. Sci.* **2015**, 8, 3022.
- [9] Z. H. Tan, X. Y. Kong, B. J. Ng, H. S. Soo, A. R. Mohamed, S. P. Chai, *ACS Omega* **2023**, 8, 1851.
- [10] R. Saini, F. Naaz, A. H. Bashal, A. H. Pandit, U. Farooq, *Green Chem.* **2024**, 26, 57.
- [11] S. Jo, K. B. Lee, J. I. Sohn, *ACS Sustainable Chem. Eng.* **2021**, 9, 14911.
- [12] Y. Chen, Y. Zhao, P. Ou, J. Song, *J. Mater. Chem. A* **2023**, 11, 9964.
- [13] K. Kawashima, R. A. Márquez, L. A. Smith, R. R. Vaidyula, O. A. Carrasco-Jaim, Z. Wang, Y. J. Son, C. L. Cao, C. B. Mullins, *Chem. Rev.* **2023**, 123, 12795.
- [14] H. Huang, A. Cho, S. Kim, H. Jun, A. Lee, J. W. Han, J. Lee, *Adv. Funct. Mater.* **2020**, 30, 2003889.
- [15] C. G. Morales-Guio, S. D. Tilley, H. Vrubel, M. Grätzel, X. Hu, *Nat. Commun.* **2014**, 5, 3059.
- [16] X. Zhang, Z. Luo, P. Yu, Y. Cai, Y. Du, D. Wu, S. Gao, C. Tan, Z. Li, M. Ren, T. Osipowicz, S. Chen, Z. Jiang, J. Li, Y. Huang, J. Yang, Y. Chen, C. Y. Ang, Y. Zhao, P. Wang, L. Song, X. Wu, Z. Liu, A. Borgna, H. Zhang, *Nat. Catal.* **2018**, 1, 460.
- [17] X. Shi, X. Zheng, H. Wang, H. Zhang, M. Qin, B. Lin, M. Qi, S. Mao, H. Ning, R. Yang, L. Xi, Y. Wang, *Adv. Funct. Mater.* **2023**, 33, 2307109.
- [18] Y. Liu, X. Liu, A. R. Jadhav, T. Yang, Y. Hwang, H. Wang, L. Wang, Y. Luo, A. Kumar, J. Lee, *Angew. Chem.* **2022**, 134, 202114160.
- [19] Y. Zhang, F. Gao, D. Wang, Z. Li, X. Wang, C. Wang, K. Zhang, Y. Du, *Coord. Chem. Rev.* **2023**, 475, 214916.
- [20] P. Kuang, T. Tong, K. Fan, J. Yu, *ACS Catal.* **2017**, 7, 6179.
- [21] V. Thirumal, R. Yuvakkumar, P. S. Kumar, G. Ravi, A. Arun, R. K. Guduru, D. Velauthapillai, *Int. J. Hydrogen Energy* **2023**, 48, 6478.
- [22] L. Yu, T. Lei, B. Nan, J. Kang, Y. Jiang, Y. He, C. T. Liu, *RSC Adv.* **2015**, 5, 82078.
- [23] a) H. Jiang, Y. Sun, B. You, *Acc. Chem. Res.* **2023**, 56, 1421; b) M. B. Kale, R. A. Borse, A. Goma Abdelkader Mohamed, Y. Wang, *Adv. Funct. Mater.* **2021**, 31, 2101313; c) H. Lan, J. Wang, L. Cheng, D. Yu, H. Wang, L. Guo, *Chem. Soc. Rev.* **2024**, 53, 684.
- [24] J. M. Huth, H. L. Swinney, W. D. McCormick, A. Kuhn, F. Argoul, *PhRvE* **1995**, 51, 3444.
- [25] B. Zeng, X. Liu, L. Wan, C. Xia, L. Cao, Y. Hu, B. Dong, *Angew. Chem., Int. Ed.* **2024**, 63, 202400582.
- [26] a) Y. Zhou, T. Li, S. Xi, C. He, X. Yang, H. Wu, *ChemCatChem* **2018**, 10, 5487; b) X. Zhang, Y. Xue, Q. Yan, K. Zhu, K. Ye, J. Yan, D. Cao, X. Huang, G. Wang, *Mater. Today Energy* **2021**, 21, 100741; c) C. Tang, H. Zhang, K. Xu, Q. Hu, F. Li, C. He, Q. Zhang, J. Liu, L. Fan, *Catal. Today* **2018**, 316, 171; d) W. Yu, Z. Chen, X. Jiang, W. Xiao, B. Dong, Z. Wu, *Int. J. Hydrogen Energy* **2022**, 47, 14414; e) Q. Xu, W. Gao, M. Wang, G. Yuan, X. Ren, R. Zhao, S. Zhao, Q. Wang, *Int. J. Hydrogen Energy* **2020**, 45, 2546; f) W. Dai, L. Lin, Y. Li, Z. Chen, F. Liu, F. Li, L. Chen, *Appl. Surf. Sci.* **2020**, 514, 145944; g) Y. Lyu, Y. Peng, *J. Electroanal. Chem.* **2023**, 947, 117755; h) Z. Ma, Q. Zhao, J. Li, B. Tang, Z. Zhang, X. Wang, *Electrochim. Acta* **2018**, 260, 82; i) F. Zhang, Y. Ge, H. Chu, P. Dong, R. Baines, Y. Pei, M. Ye, J. Shen, *ACS Appl. Mater. Interfaces* **2018**, 10, 7087; j) J. Yao, L. Bai, X. Ma, M. Zhang, L. Li, G. Zhou, H.

- Gao, *ChemCatChem* **2019**, *12*, 609; k) X. Wang, W. Ma, C. Ding, Z. Xu, H. Wang, X. Zong, C. Li, *ACS Catal.* **2018**, *8*, 9926; l) F. Wu, X. Guo, G. Hao, Y. Hu, W. Jiang, *J. Solid State Electrochem.* **2019**, *23*, 2627; m) C. Hu, Q. Ma, S. F. Hung, Z. N. Chen, D. Ou, B. Ren, H. M. Chen, G. Fu, N. Zheng, *Chem* **2017**, *3*, 122; n) M. Hosseini, T. Shahrabi, G. B. Darband, A. Fathollahi, *Langmuir* **2024**, *40*, 2028; o) Z. Zang, Q. Guo, X. Li, Y. Cheng, L. Li, X. Yu, Z. Lu, X. Yang, X. Zhang, H. Liu, *J. Mater. Chem. A* **2023**, *11*, 4661; p) S. Zhu, J. Lei, S. Wu, L. Liu, T. Chen, Y. Yuan, C. Ding, *Mater. Lett.* **2022**, *311*, 131549.
- [27] J. Zhu, L. Hu, P. Zhao, L. Y. S. Lee, K. Y. Wong, *Chem. Rev.* **2019**, *120*, 851.
- [28] S. S. Jeon, P. W. Kang, M. Klingenhof, H. Lee, F. Dionigi, P. Strasser, *ACS Catal.* **2023**, *13*, 1186.
- [29] J. N. Hansen, H. Prats, K. K. Toudahl, N. Mørch Secher, K. Chan, J. Kibsgaard, I. Chorkendorff, *ACS Energy Lett.* **2021**, *6*, 1175.
- [30] D. Merki, S. Fierro, H. Vrubel, X. Hu, *Chem. sci.* **2011**, *2*, 1262.
- [31] J. Wang, J. Hu, S. Niu, S. Li, Y. Du, P. Xu, *Small* **2022**, *18*, 2105972.
- [32] J. P. Perdew, Y. Wang, *Phys. Rev. B* **1992**, *45*, 13244.
- [33] G. Kresse, J. Furthmüller, *Phys. Rev. B* **1996**, *54*, 11169.
- [34] a) P. E. Blöchl, *Phys. Rev. B* **1994**, *50*, 17953; b) G. Kresse, D. Joubert, *Phys. Rev. B* **1999**, *59*, 1758.
- [35] S. Grimme, J. Antony, S. Ehrlich, H. Krieg, *J. Phys. Chem. C* **2010**, *132*, 154104.
- [36] G. Kresse, J. Hafner, *Phys. Rev. B* **1993**, *47*, 558.
- [37] S. Nosé, *J. Phys. Chem. C* **1984**, *81*, 511.
- [38] a) Y. Luo, X. Li, X. Cai, X. Zou, F. Kang, H. M. Cheng, B. Liu, *ACS Nano* **2018**, *12*, 4565; b) B. Zhang, J. Liu, J. Wang, Y. Ruan, X. Ji, K. Xu, C. Chen, H. Wan, L. Miao, J. Jiang, *Nano Energy* **2017**, *37*, 74.
- [39] J. K. Nørskov, J. Rossmeisl, A. Logadottir, L. Lindqvist, J. R. Kitchin, T. Bligaard, H. Jonsson, *J. Phys. Chem. B* **2004**, *108*, 17886.
- [40] L. I. Bendavid, E. A. Carter, *J. Phys. Chem. C* **2013**, *117*, 26048.